Fisher Information-Based Evaluation of Image Quality for Time-of-Flight PET

Kathleen Vunckx, Lin Zhou, Samuel Matej, Michel Defrise and Johan Nuyts

Abstract— **The use of time-of-flight (TOF) information during reconstruction is generally considered to improve the image quality. In this work we quantified this improvement using two existing methods: (1) a very simple analytical expression only valid for a central point in a large uniform disk source, and (2) efficient analytical approximations for post-filtered maximum likelihood expectation maximization (MLEM) reconstruction with a fixed target resolution, predicting the image quality in a voxel or in a small region based on the Fisher information matrix. The image quality was investigated at different locations in various software phantoms. Simplified as well as realistic phantoms, measured both with TOF positron emission tomography (PET) systems and with a conventional PET system, were simulated. Since the time resolution of the system is not always accurately known, e.g. it might be dependent on the count rate, the effect on the image quality of using an inaccurate kernel during reconstruction was also examined using the Fisher information-based method. First, we confirmed with this method that the variance improvement in the center of a large uniform disk source is proportional to the disk diameter and inversely proportional to the time resolution. Next, image quality improvement was observed in all pixels, but in central and low-count regions the contrast-to-noise ratio (CNR) increased faster than in eccentric or high-count regions. Finally, the CNR was seen to decrease when an inaccurate time resolution (too narrow as well as too wide) was used during reconstruction. Although the optimum is rather flat, using an inaccurate kernel might introduce artifacts in the reconstructed image.**

I. Introduction

In the 1980s a great research interest emerged for the use of time-of-flight (TOF) information in positron emission tomography (PET). However, due to the lack of fast scintillators with a high efficiency, this promissing route was deserted until in the 1990s the development of new scintillators, such as lutetium orthosilicate (LSO) and lanthanum bromide ($LaBr_3$), renewed the interest in TOF PET. The effect on the image quality of using TOF information during PET reconstruction has been studied extensively by many groups. It has been shown with analytical calculations (e.g. [1]), (Monte Carlo) simulations (e.g. [2]) and experimental data (e.g. [3]) that the image quality increases with TOF PET compared to non-TOF PET. Most of the gain induced by TOF is obtained by a reduced variance. Many analytical approaches to predict the image quality are, however, restricted to simple objects. In addition, simulations and experiments are very time-consuming and/or give noisy results due to low-count statistics.

In this work, we use an analytical method, based on the Fisher information matrix, to predict the impulse response and the covariance in individual pixels of three phantoms imaged with various 2D TOF PET systems, as well as with a conventional PET system.

During reconstruction, the finite TOF resolution is usually modeled as a Gaussian with full-width at half-maximum (FWHM) Δt, or equivalently $\Delta x (= c\Delta t/2)$, with Δx the localization uncertainty of the TOF PET system, c the speed of light, and Δt the time resolution. This Gaussian is often called the TOF kernel. We studied the effect of using an inaccurate TOF kernel, because (1) Δt is not always known accurately, (2) Δt might be dependent on the count rate [4], and (3) surprisingly a wider kernel was found to improve the image quality in [5].

II. Theory

A. Previous Analytical Calculation Gain due to TOF

In 1981, Tomitani derived a formula to evaluate the variance of a central pixel in a uniform disk source with diameter D, reconstructed with a filtered back-projection (FBP) method using TOF information [1]. He proved that confidence weighted FBP ensures minimal variance, and calculated the variance reduction due to TOF:

$$V_{TOF,min} = \frac{c^2}{8}\frac{a\Delta x}{\Delta r^3} \tag{1}$$

and

$$\frac{V_{non-TOF,min}}{V_{TOF,min}} = \frac{c}{2\sqrt{\pi}}\frac{D}{\Delta x} = 0.66\frac{D}{\Delta x} \tag{2}$$

with $c = \sqrt{8\ln 2}$, a the amount of detected coincidences per cm^2, and Δr the resolution of the reconstructed image, (both Δx and Δr express the full-width at half-maximum (FWHM)).

Because of the symmetry of the phantom, these expressions also hold for weighted least squares reconstruction. Consequently, they also apply to maximum a posteriori (MAP) or post-smoothed maximum likelihood expectation maximization (MLEM) in cases where the non-negativity constraint can be ignored.

B. Fisher Information-Based Image Quality Prediction

K. Vunckx, L. Zhou an J. Nuyts are with the Dept. of Nuclear Medicine, K.U.Leuven, B-3000 Leuven, Belgium. S. Matej is with the Dept. of Radiology, Univ. of Pennsylvania, Philadelphia, PA 19104 USA. M. Defrise is with the Dept. of Nuclear Medicine, V.U.Brussel, B-1090 Brussel, Belgium.

This work is supported by F.W.O. grant G.0569.08, K.U.Leuven grant IDO/02/012, I.W.T. grant SBO - ANIMONE and an IEEE MIC travel grant.

1) Basic Equations: In emission tomography, the linearized local impulse response (LLIR) and the covariance in a reconstructed pixel are often used as image quality measures. In [6], [7] efficient analytical approximations for the LLIR and the covariance of a pixel j were proposed for converged MAP reconstruction:

$$l^j(\Lambda) \approx [\boldsymbol{F} + \beta \boldsymbol{U}]^{-1} \boldsymbol{F} e^j \tag{3}$$

$$\mathrm{Cov}^j(\Lambda) \approx [\boldsymbol{F} + \beta \boldsymbol{U}]^{-1} \boldsymbol{F} [\boldsymbol{F} + \beta \boldsymbol{U}]^{-1} e^j \tag{4}$$

where $\boldsymbol{F}$ is the Fisher information matrix, which (in emission tomography) can be calculated by a projection followed by a weighted backprojection, β is the smoothing parameter, $\boldsymbol{U}$ is the Hessian of the quadratic prior, used for regularization, and e^j the j-th unit vector.

Assuming local shift-invariance, equations (3) and (4) can be calculated by convolutions in the spatial domain, or - more efficiently - by multiplications in the Fourier domain [7].

To enable comparison between different systems at equal (uniform) spatial resolution, we adapted the above equations to approximate post-smoothed MLEM [8]. Essentially, we assumed $[\boldsymbol{F} + \beta \boldsymbol{U}]^{-1}$ could be approximated by $\boldsymbol{P}^j \boldsymbol{G}^j$, with $\boldsymbol{P}^j$ an isotropic Gaussian post-smooth filter that tries to impose the given target resolution and $\boldsymbol{G}^j$ the approximate pseudoinverse of the local shift-invariant approximation $\boldsymbol{F}^j$ of the Fisher information matrix (all j-dependent). Equations (3) and (4) then become:

$$l^j(\Lambda) \approx \boldsymbol{P}^j \boldsymbol{G}^j \boldsymbol{F}^j e^j \tag{5}$$

$$\mathrm{Cov}^j(\Lambda) \approx \boldsymbol{P}^j \boldsymbol{G}^j \boldsymbol{F}^j \boldsymbol{G}^{jT} \boldsymbol{P}^j e^j \tag{6}$$

where ^{T} denotes transpose.

The j-th element of $l^j(\Lambda)$ and $\mathrm{Cov}^j(\Lambda)$ are the contrast recovery coefficient (CRC) and the variance in pixel j, respectively. Combined they yield the contrast-to-noise ratio (CNR), often used as an image quality measure:

$$\mathrm{CNR} = \frac{\mathrm{CRC}}{\sqrt{\mathrm{Var}}}. \tag{7}$$

2) Extension to Regions of Interest: Since local shift-invariance was assumed, the filters found for individual pixels (see (5) and (6)) are circulant matrices and they can therefore be applied to all pixels of a small region of interest (ROI). The approximations for the post-smoothed LLIR and the variance of the ROI are then

$$LLIR^{ROI} \approx Q_I \begin{bmatrix} 0 \\ \vdots \\ 1/r \\ 1/r \\ 1/r \\ \vdots \\ 0 \end{bmatrix} \tag{8}$$

$$Var^{ROI} \approx \begin{bmatrix} 0 \dots \frac{1}{r} \frac{1}{r} \frac{1}{r} \dots 0 \end{bmatrix} Q_V \begin{bmatrix} 0 \\ \vdots \\ 1/r \\ 1/r \\ 1/r \\ \vdots \\ 0 \end{bmatrix} \tag{9}$$

with $Q_I = \boldsymbol{P}^j \boldsymbol{G}^j \boldsymbol{F}^j$, $Q_V = \boldsymbol{P}^j \boldsymbol{G}^j \boldsymbol{F}^j \boldsymbol{G}^{jT} \boldsymbol{P}^j$, and r the number of pixels in the ROI.

3) Extension to Mismatched TOF Kernels: We can easily include the reconstruction TOF kernel in (5) and (6). First, we substitute $\boldsymbol{F}^j$ by $\boldsymbol{A}^{\boldsymbol{T}j} \boldsymbol{C}_{\boldsymbol{Y_A}}^{-\boldsymbol{1}} \boldsymbol{A}^j$, with $\boldsymbol{A}^j$ and $\boldsymbol{A}^{\boldsymbol{T}j}$ the forward and backward projection matrix, respectively, with the correct kernel (i.e. in agreement with the measurement). $\boldsymbol{C}_{\boldsymbol{Y_A}}^{-\boldsymbol{1}}$ represents the covariance matrix of the phantom measurement. Next, we identify which projection and backprojection operations need to model the real measurements, and which need to model the reconstruction. In the latter case, $\boldsymbol{A}^j$ and $\boldsymbol{A}^{\boldsymbol{T}j}$ are substituted by $\boldsymbol{B}^j$ and $\boldsymbol{B}^{\boldsymbol{T}j}$, respectively, which represent the forward and backward projection matrix, respectively, modeling the TOF kernel with the inaccurate time resolution. This yields:

$$l^j(\Lambda) \approx \boldsymbol{P}^j [\boldsymbol{A}^{\boldsymbol{T}j} \boldsymbol{C}_{\boldsymbol{Y_A}}^{-\boldsymbol{1}} \boldsymbol{A}^j]^{-1} \boldsymbol{A}^{\boldsymbol{T}j} \boldsymbol{C}_{\boldsymbol{Y_A}}^{-\boldsymbol{1}} \boldsymbol{A}^j e^j \tag{10}$$

$$\approx \boldsymbol{P}^j [\boldsymbol{B}^{\boldsymbol{T}j} \boldsymbol{C}_{\boldsymbol{Y_A}}^{-\boldsymbol{1}} \boldsymbol{B}^j]^{-1} \boldsymbol{B}^{\boldsymbol{T}j} \boldsymbol{C}_{\boldsymbol{Y_A}}^{-\boldsymbol{1}} \boldsymbol{A}^j e^j \tag{11}$$

$$\mathrm{Cov}^j(\Lambda) \approx \boldsymbol{P}^j [\boldsymbol{A}^{\boldsymbol{T}j} \boldsymbol{C}_{\boldsymbol{Y_A}}^{-\boldsymbol{1}} \boldsymbol{A}^j]^{-1} \boldsymbol{A}^{\boldsymbol{T}j} \boldsymbol{C}_{\boldsymbol{Y_A}}^{-\boldsymbol{1}} \boldsymbol{A}^j ([\boldsymbol{A}^{\boldsymbol{T}j} \boldsymbol{C}_{\boldsymbol{Y_A}}^{-\boldsymbol{1}} \boldsymbol{A}^j]^{-1})^T \boldsymbol{P}^j e^j \tag{12}$$

$$\approx \boldsymbol{P}^j [\boldsymbol{B}^{\boldsymbol{T}j} \boldsymbol{C}_{\boldsymbol{Y_A}}^{-\boldsymbol{1}} \boldsymbol{B}^j]^{-1} \boldsymbol{B}^{\boldsymbol{T}j} \boldsymbol{C}_{\boldsymbol{Y_A}}^{-\boldsymbol{1}} \boldsymbol{B}^j ([\boldsymbol{B}^{\boldsymbol{T}j} \boldsymbol{C}_{\boldsymbol{Y_A}}^{-\boldsymbol{1}} \boldsymbol{B}^j]^{-1})^T \boldsymbol{P}^j e^j. \tag{13}$$

III. Simulations

A. Homogeneous Disk, no Attenuation

For the first experiment, two homogeneous disk phantoms with a diameter of 20 cm and 35 cm were simulated in order to mimic a 2D slice of a slim and a heavy patient, respectively. The reconstruction image quality in the central pixel obtainable with 12 different idealized 2D TOF PET tomographs with a time resolution Δt ranging from 100 to 1500 ps FWHM, and with a conventional PET system was examined. For each system, the variance in this pixel was calculated twice, first from the approximation derived by Tomitani (2) and second from the Fisher information-based approximation (6).

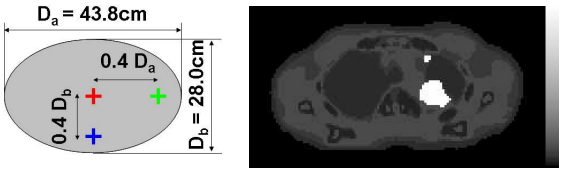

(a) (b)

Fig. 1. Illustration (a) of the dimensions of the water-filled ellipse and the location of the investigated points, and (b) of the realistic 2D thorax phantom (activity distribution).

The simulations produced sinograms of size 336x336(x84) (detector pixels x projection angles (x time bins)) for (TOF) PET. The image space consisted of 336x336 square pixels of 0.2 cm. Post-smoothing ensured a resolution of 0.6 cm FWHM. Attenuation, scatter, randoms and detector resolution were not modeled.

B. Homogeneous Ellipse

Since 2D transaxial slices of a patient are usually more ellipse-shaped and attenuation is not negligible, a water-filled ($\mu = 0.096$ cm^{-1}) elliptical phantom with the same area as the 35 cm diameter disk phantom was simulated. The long axis-to-short axis diameter ratio (D_a/D_b) was taken 1.56, which results in a D_a and D_b of 43.8 and 28.0 cm, respectively. The variance was examined using (6) in three points: the central pixel and a pixel at a distance from the center of 80% of $D_a/2$ and $D_b/2$, respectively (see Fig. 1(a)).

The same TOF and non-TOF PET systems were simulated as for the previous phantom. Also the image parameters were left unchanged. Again scatter, randoms and detector resolution were not modeled.

C. Realistic 2D Thorax Phantom

To get a feeling of the gain that can be expected from imaging a real patient with a TOF PET system, a 2D thorax phantom with realistic activity distribution and attenuation values was simulated (see Fig. 1(b)). The phantom was obtained by tresholding the CT image of a clinical FDG-PET/CT scan of a patient with several tumors in the lungs. Regions with a similar amount of Hounsfield units were assigned the same linear attenuation coefficient. Next, these regions were given a realistic uptake value, based on the corresponding values in the PET image.

The image quality of the thorax phantom was compared for two systems, i.e. a TOF PET system with a time resolution of 500 ps FWHM and a conventional PET system. The variance image for each PET system was obtained in two different manners. First, the variance was calculated in each pixel using (6). Next, the variance image was derived from the post-smoothed MLEM reconstruction of 300 projection data sets of the phantom corrupted with semi-random Poisson noise. The MLEM reconstructions were speeded-up using reduced ordered subsets [9]. An equivalent of 214 iterations over the complete data set were executed. Dividing the variance image of the non-TOF by that of the TOF PET system will show the variance improvement (also called gain in the rest of the paper) throughout the phantom.

The intrinsic resolution of the detector was taken 0.5 cm FWHM. The sinograms were of size 192x192x96 for TOF and 192x192 for non-TOF PET. The image space had 192x192 square pixels of 0.3375 cm. The target resolution was 1.2 cm FWHM. No scatter nor randoms were modeled.

D. Effect of TOF Kernel Accuracy

As a last simulation study, the effect on the image quality of modeling the time resolution with an inaccurate kernel during reconstruction is investigated. Because we want to compare the results of our study (obtained with the Fisher information-based method) to those presented in [5] (based on the reconstruction of noisy projection data sets), the simulation parameters were taken as similar as possible. Since in this work the contrast is directly obtained from the impulse response, a homogeneous disk phantom of 27 cm diameter is simulated instead of a hot-spheres phantom (of the same size). The mean and the variance on the mean in a 1.3 cm diameter ROI at 7 cm from the center were then calculated from (8) and (9). The CNR can simply be derived from these two values (see (7)).

The time resolution of the simulated TOF PET scanner was modeled as a Gaussian with a FHWM of 300 ps. The image quality obtained with a variety of reconstruction TOF kernel resolutions, i.e. 150, 225, 300, 375, 450, and 600 ps FWHM, was evaluated using (11) and (13). The attenuation of water was modeled, but scatter, randoms and detector resolution were not considered. The dimensions of the sinogram and of the image space were 336x336x48 and 336x336, respectively. The pixel size was taken 0.2x0.2 mm^2 and a target resolution of 0.6 cm FWHM was imposed.

IV. Results

A. Homogeneous Disk, no Attenuation

In figure 2, the variance improvement in the central pixel of both the 20 cm (solid lines) and the 35 cm (dotted lines) diameter uniform disk source obtained due to the use of TOF information is plotted with respect to the time resolution Δt of the TOF PET systems. Two prediction methods are compared: (1) Tomitani's approximation (results drawn in black) and (2) the Fisher information-based method (results plotted in red). The predictions of the two methods closely match. The accuracy is better for good time resolutions and for a large diameter. The approximation of Tomitani predicts that for smaller phantoms the image quality is better using a conventional PET system than using a TOF PET system with bad time resolution. This is due to the fact that the assumptions made during the derivation of (2) are no longer valid.

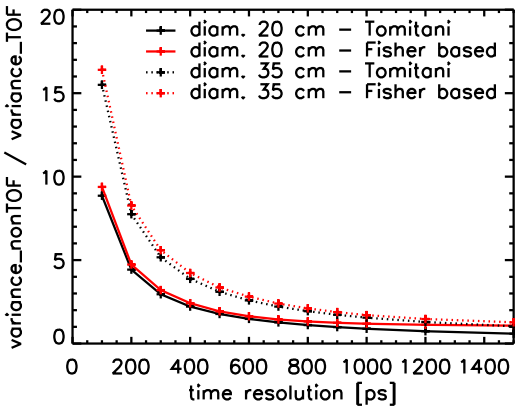

Fig. 2. Simulation 1: Variance improvement due to the use of TOF information plotted versus the time resolution of the TOF PET systems. The image quality of the central pixel of two uniform disk phantoms with a diameter of 20 (solid lines) and 35 cm (dotted lines), respectively, was investigated with two methods: (black) the method proposed by Tomitani (see (2)), and (red) the Fisher information-based method (see (6)).

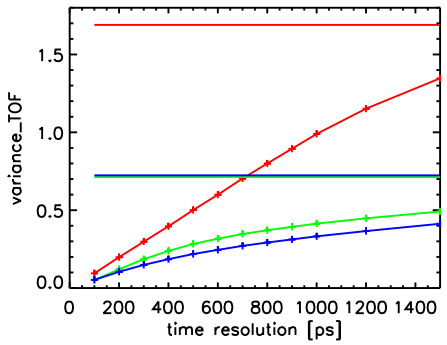

Fig. 3. Simulation 2: Variance in 3 points of a homogeneous water-filled ellipse is plotted with respect to the time resolution (in picoseconds FWHM) of the tested systems. The horizontal lines show the results for the conventional PET system. The long and short axis diameter is 43.8 cm and 28.0 cm, respectively. The central pixel (red), the eccentric pixel on the long axis (green) and on the short axis (blue) were investigated.

B. Homogeneous Ellipse

Figure 3 plots the variance for the three pixels in the water-filled ellipse versus the time resolution of the TOF PET systems. The horizontal lines depict the variance obtained with the conventional PET system. For all PET systems the variance in the central pixel (red) is clearly higher than the variance in the eccentric pixels (green and blue). The variance in the eccentric pixel on the short axis (blue) is slightly lower than that on the long axis (green) if TOF information is used during reconstruction. For perfect time resolution their variance converges to the same value.

The evolution of the improvement in variance in the three points is denoted in table I. The gain was shown for current generation, next generation and future generation TOF PET systems with a time resolution of 1500, 500 and 100 ps, respectively. The eccentric pixels start to benefit from the TOF information already at modest time resolutions (factors 1.45 and 1.75 for eccentric points vs. a factor 1.25 for the central one at Δt =1500 ps), but the variance decreases faster with improved time resolution in the central pixel (gain close to 18 for the central pixel vs. nearly 14 for the eccentric ones).

TABLE I

VARIANCE IMPROVEMENT IN THREE POINTS OF A WATER-FILLED ELLIPSE.

Δt	100 ps	500 ps	1500 ps
Central point	17.85	3.37	1.25
Point at $0.4D_a$	13.90	2.52	1.45
Point at $0.4D_b$	13.73	3.31	1.75

C. Realistic 2D Thorax Phantom

The calculated variance and gain images of the thorax phantom (see Fig. 1(b)) are shown in Fig. 4. The left column contains the variance and gain images predicted with the Fisher information-based method, in the right column the corresponding images obtained from the reconstruction of 300 noisy projection data sets are shown. The variance images expected from the TOF PET system with $\Delta t = 500$ ps FHWM are shown on the first row. The variance images predicted for the conventional PET system can be seen on the middle row. The last row illustrates the distribution of the variance improvement over the thorax phantom, calculated with both methods.

From the first two rows it is clear that the variance reduces when TOF information is available during reconstruction. As Δt decreases the variance images look more and more similar to the thorax image (see Fig. 1(b)), because imaging with excellent time resolution results in an image of the phantom corrupted by Poisson noise. From the gain images (see Fig. 4E and F), we can conclude that the variance reduces faster in the low-active lungs than in the high-active tumors. The predictive value of the approximate method is very good, except in low-active regions.

D. Effect of TOF Kernel Accuracy

In Fig. 5, the mean (left), the variance on the mean (center) and the CNR of the ROI (right) are plotted with respect to the reconstruction TOF kernel. The top row shows the results for the standard case, where $\boldsymbol{P}^j$ was the Gaussian post-smooth filter that imposes the 6 mm FWHM target resolution. As can be seen, both the mean and the variance increase with increasing kernel width. When the kernel was taken too narrow ($<$ 300 ps), the mean decreased faster than the variance. On the contrary, when the kernel was take too wide ($>$ 300 ps), the mean increased slower than the variance. As a result, the best contrast versus variance trade-off was obtained using the correct kernel (300 ps FWHM).

One should note, however, that - due to the fixed target resolution - the mean value in the ROI was expected to be constant. The fact that it is not, can be explained by investigating the shape of the post-smoothed impulse response. For the

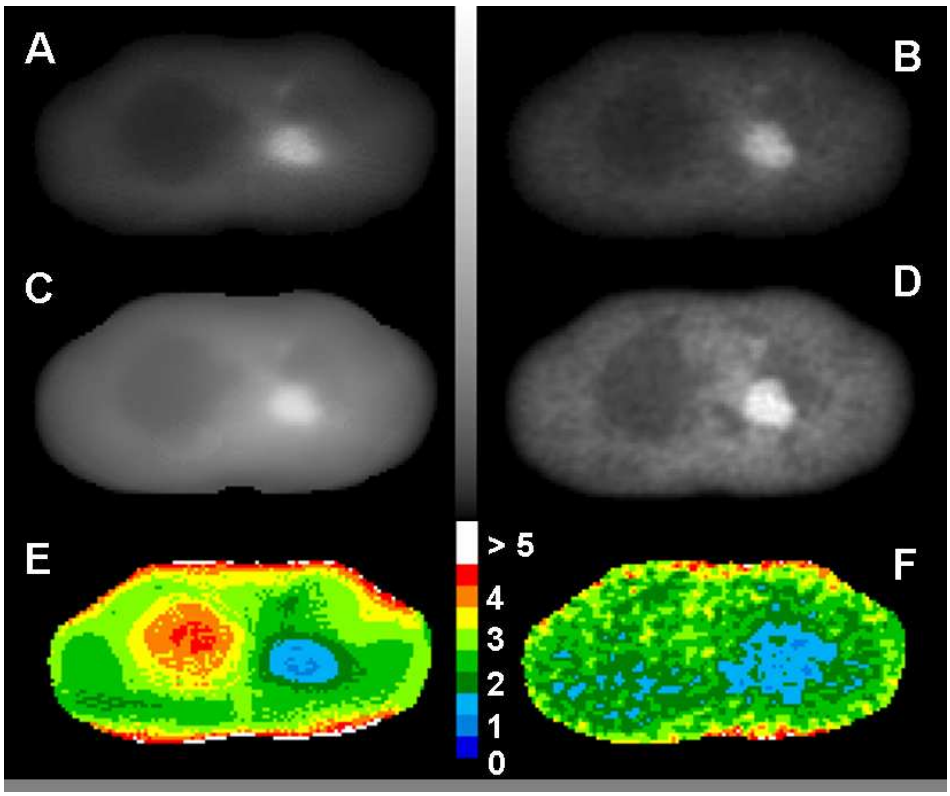

Fig. 4. Simulation 3: Evaluation of the effect of the use of TOF PET for a realistic 2D thorax phantom. Variance images expected for a TOF PET system with a time resolution of 500 ps FWHM (top row) and for a conventional PET system (middle row) were obtained with the Fisher information-based method (first column) as well as with the reconstruction of 300 noisy projection data sets (second column). From these variance images the corresponding distribution of the variance improvement was calculated (bottom row).

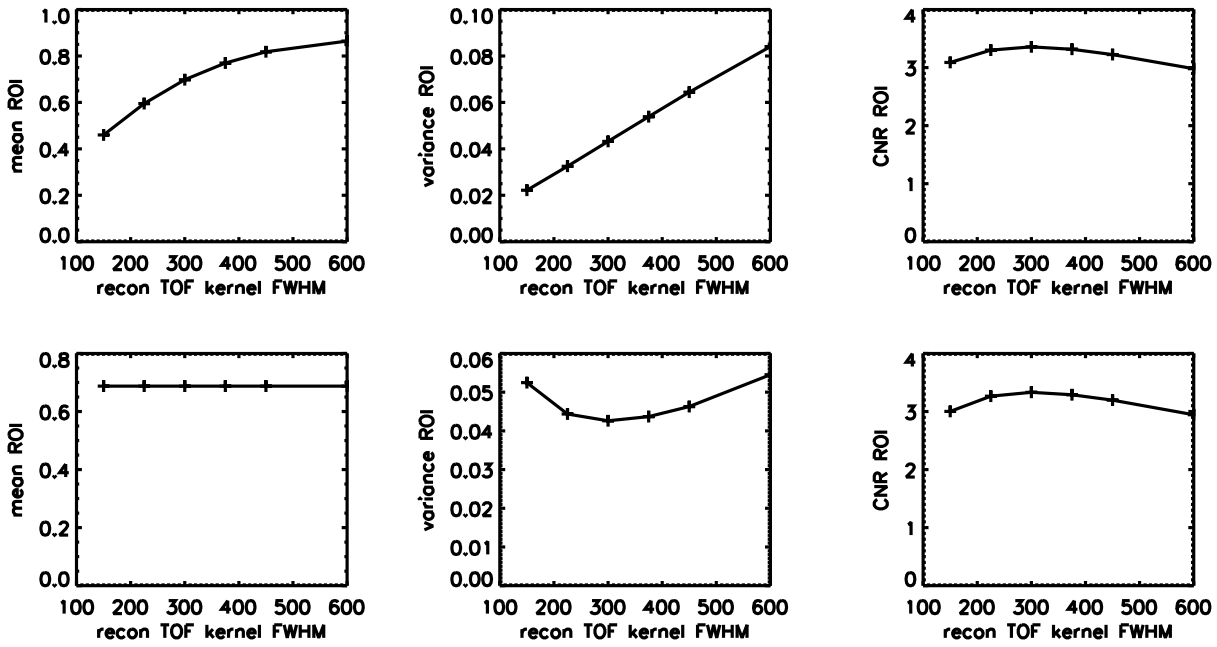

Fig. 5. Simulation 4: Mean, variance on the mean, and CNR of the eccentric ROI in the 27 cm diameter homogeneous sphere (described in section III-D) plotted with respect to the TOF kernel used during reconstruction. The real TOF kernel had a resolution of 300 ps. Top: Gaussian post-filter. Bottom: optimal post-filter.

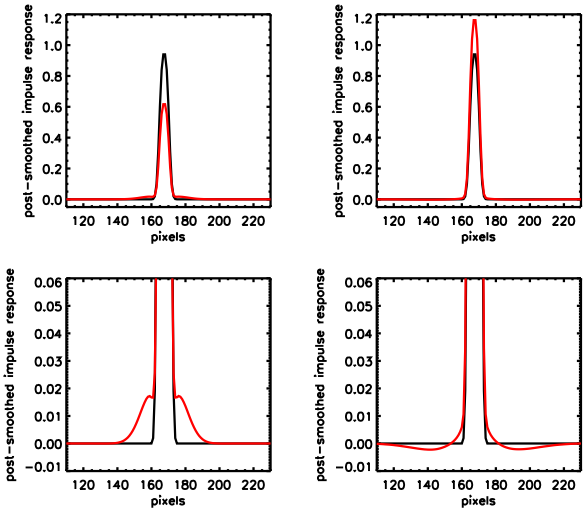

Fig. 6. Simulation 4: Illustration of the artifacts in the post-smoothed impulse response caused by using an inaccurate TOF kernel during reconstruction. The black lines show the ideal post-smoothed impulse response, obtained by post-smoothing the ROI (all values of ROI equal to 1) with a Gaussian with a FWHM of 6 mm (target resolution). The red line plots the post-smoothed impulse response obtained with a too narrow kernel (left) and a too wide kernel (right), respectively. Top row: full range. Bottom row: zoomed-in on bottom part of impulse response.

narrowest and widest kernel, profiles of these are drawn in red in the left and right top graph of Fig. 6, respectively. The black curve represents the impulse in the ROI after post-smoothing with a Gaussian filter with 6 mm FWHM. From the top images a clear under- and overshoot can be remarked for the narrow and wide kernel, respectively. Correspondingly, sidelobes and undershoots outside the FWHM range can be observed in the bottom row images, which are a zoomed-in version of the top ones.

To force the mean value in the ROI to be constant, $\boldsymbol{P}^j$ should ensure both the shape and the resolution of the post-smoothed impulse response to agree with a ROI (with all elements set to 1) post-smoothed with the target Gaussian filter. The results obtained with this optimal post-filter are shown on the bottom row of Fig. 5. Again the mean, the variance and the CNR of the ROI were plotted versus the reconstruction TOF kernel. Obviously, the mean of the ROI is now fixed and equal to the value obtained with the 300 ps FWHM reconstruction kernel and Gaussian post-smoothing (see top left graph of the same image). All effects of the reconstruction kernel accuracy are now contained by the variance, or equivalently, by the CNR. A very similar CNR curve, with the same optimum, was found using the optimal post-filter instead of the Gaussian post-smooth filter.

V. Discussion

Tomitani's approximation was - as expected - most accurate for good time resolutions and for central pixels in a large object, because he introduces some approximations only valid for an infinitely large object. However, in these approximations the effects of attenuation, randoms, etc. cannot be included.

As TOF information reduces the randoms fraction significantly, even larger gains might be within reach. The effect of randoms on the image quality of TOF PET was discussed in [10], based on experimental data and an extended version of the $\sqrt{D/\Delta t}$ rule was proposed. In the Fisher information-based method simple models for randoms, scatter, etc. can easily be included to study their effect on the image quality. It is also readily extensible to 3D TOF PET.

For conventional PET the variance was already lower in an eccentric pixel than in a central one, because the mean intersection length between object and the projection lines through the pixel, such that the measured activity can be spread over less pixels and activity from surrounding pixels is less deposited in the investigated pixel. This advantage reduces with improved time resolution of the TOF PET system.

In Fig. 4E and F the variance in the lung is seen to decrease faster than the variance in the rest of the thorax. This can be explained as follows. In conventional PET the measured activity is backprojected along the complete line-of-response. However most of the activity deposited in the lung did not originate form the lung, but from e.g. the tumor. In TOF PET, the activity of the tumor will only be backprojected in the neighborhood of the tumor with a weight decreasing with increasing distance from the originating point.

The analytical approximations, based on the calculation of the Fisher information matrix, predict accurately the image quality of post-filtered MLEM reconstructions. Only for pixels or ROIs with very low activity, this approximate method underestimates the image quality that can be attained by post-filtered MLEM. The latter has the advantage of being bounded by the non-negativity constraint, whereas the approximations represent a linearized model of the reconstruction. The inconsistency can be observed in the variance images of the 2D thorax phantom, where higher variance is predicted (see Fig. 4A and C) in the low-active lungs than was found from repeated MLEM reconstructions (see Fig. 4B and D). The inaccuracy was most prominent for conventional PET. Therefore, the gain in the lungs was overestimated by the Fisher information-based method.

The efficiency of the Fisher information-based method allows rapid evaluation of the effect of different parameters (such as the object shape, the attenuation, the time resolution and the randoms fraction) on the reconstruction image quality of a few individual pixels or ROIs. To obtain complete variance images faster methods are available [11]. To speed-up the calculation of the variance images, the pixel size was increased from 0.2 cm to 0.3375 cm, which is still clinically relevant. Correspondingly, the target resolution was increased, because a minimal amount of post-smoothing is required for stability and accuracy of the approximations.

The kernel mismatch between measurement and reconstruction could easily be incoorporated in the approximations (see (10)-(13)). Though, their use is subject to some restric-

tions. In cases where the reconstruction TOF kernel FWHM is larger than the real time resolution, problems might occur due to the factor $\boldsymbol{C}_{\boldsymbol{Y_A}}^{-1}$, because then the projection of the impulse in a pixel or small ROI, which was filtered with the reconstruction TOF kernel, has to be divided by the projection of the phantom, which was filtered with the real, narrower TOF kernel. Consequently, the tails of the TOF kernel might be divided by a very small number (in order not to divide by zero), because the activity of the point is spread further than the activity of the phantom. This results first in asymmetric undershoot artifacts, as shown in the right image of Fig. 7., which shows the (zoomed-in) profile in the column direction through the center of the predicted post-smoothed impulse response, obtained with the 600 ps FWHM TOF reconstruction kernel (the real kernel was 300 ps). For more eccentric pixels or larger resolution differences, the approximations become increasingly inaccurate or even instable. Careful use of these approximations is therefore recommended.

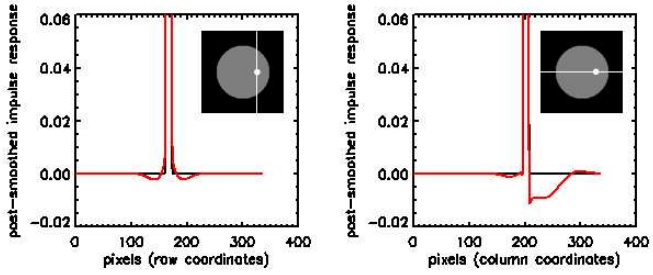

Fig. 7. Illustration of asymmetric undershoot artifacts. The left graph is identical to the bottom right plot of Fig. 6, except for the x-range. It represents the (zoomed-in) profile in the row direction through the center of the post-smoothed impulse response of the eccentric ROI. The right graph shows the profile in the column direction.

From the curves in the top row of Fig. 5, we found that the mean value in the ROI, and thus also the contrast, decreases if the reconstruction kernel is chosen too narrow, and increases when the kernel is taken too wide. This is in agreement with the findings in [5]. However, from the same experiment we could also conclude that the CNR is optimal when using the correct kernel during reconstruction, whereas in [5] the increased contrast seemed to overcompensate the increase in noise. The main difference between the two methods are the way the figure-of-merit (FOM) for the noise is calculated, and the reconstruction method used/approximated. The noise was determined from the pixel-to-pixel percent standard deviation (%SD) in background ROIs, averaged over 60 background ROI. The variance (or standard deviation) on the mean value of the ROI is considered to be a more accurate and more representative noise FOM. In [5] the image quality was evaluated after different numbers of iterations, but no matched resolution was assured, which makes it very difficult to compare image quality. Also convergence speed might differ for different TOF kernels. In this work, we preferred post-smoothing MLEM reconstructions, run until convergence, to overcome these difficulties.

The CNR curves in the right column of Fig. 5 indicate that small deviations from the real kernel, and thus also from the effective time resolution, only have a minor effect on the image quality. However, these inaccuracies also induce artifacts in the reconstruction image, because the measured activity needs to be explained by a different model than the one of the measurement. For kernels that are too narrow, some of the original activity is deposited in side lobes (see Fig. 6, left column). This is necessary to explain the activity measured at a larger distance from the correct detection point than the reconstruction TOF kernel can spread the activity. For kernels that are too wide, the activity is assigned to a smaller ROI than in reality (see Fig. 6, right column). The undershoots are needed to cancel the activity that is projected on the detectors at a large distance from the exact projection location, but that was not measured, since the real TOF kernel is more narrow. In both cases (too narrow and too wide) not only edge effects are to be expected, but also the quantification will be incorrect. This is also illustrated in Fig. 8, where three reconstruction images of the same noiseless projection data set are shown. The software phantom described in section III-D was measured with a TOF PET system with a time resolution of 300 ps FWHM. The activity in the eccentric ROI was doubled compared to the background activity. The post-smoothed MLEM reconstruction was done with 214 reduced ordered subsets and a TOF kernel with a FWHM of 150, 300, and 600 ps was used to obtain Fig. 8(a), (b) and (c), respectively. In Fig. 8(d) the horizontal profiles through the center of the ROI are plotted for the too narrow (red), correct (black) and too wide (green) TOF kernel. The same artifacts as found in Fig. 6 can be recognized. We can also conclude that the artifacts due to the use of a too narrow kernel are much more localized than the once caused by the too wide kernel. In [12] similar artifacts were observed after reconstruction of simulated TOF PET data with mismatched TOF kernels. The degree of importance of these artifacts in reconstruction images of measured data is still to be verified.

VI. Conclusion

Analytical Fisher information-based approximations were used to evaluate the image quality of simple and more realistic phantoms imaged with 2D TOF PET systems with different time resolutions and to compare it with the image quality obtained with a conventional PET system. TOF information was found to improve the image quality in all pixels, but more benifit was seen in central and low-count regions. Using a too narrow or too wide TOF kernel for reconstruction tends to decrease the image quality and might cause artifacts in the reconstructed image.

References

[1] T. Tomitani, "Image reconstruction and noise evaluation in photon time-of-flight assisted positron emission tomography." *IEEE Trans. Nucl. Sci.*, vol. 28(6), pp. 4582-4589, 1981.

[2] S. Surti, J. S. Karp, and G. Muehllehner, "Image quality assessment of $LaBr_3$-based whole-body 3D PET scanners: a Monte Carlo evaluation." *Phys. Med. Biol.*, vol. 49(19), pp. 4593-4610, 2004.

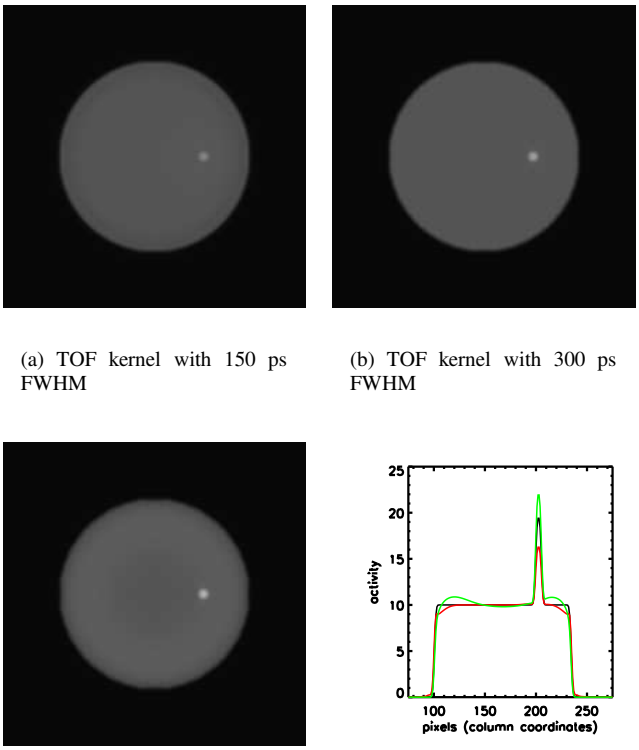

(a) TOF kernel with 150 ps FWHM

(b) TOF kernel with 300 ps FWHM

(c) TOF kernel with 600 ps FWHM

(d) Horizontal profiles

Fig. 8. Homogeneous 27 cm diameter disk with an impulse in a 1.3 cm diameter ROI at 7 cm from the center, after reconstruction with a TOF kernel with a FWHM of (a) 150 ps, (b) 300 ps, and (c) 600 ps. In (d) the respective horizontal profiles through the center of the ROI are plotted in red (150 ps), black (300 ps) and green (600 ps).

[3] M. Yamamoto, D. C. Ficke, and M. M. Ter-Pogossian, "Experimental assessment of the gain achieved by the utilization of time-of-flight information in a positron emission tomograph (Super PETT I)." *IEEE Trans. Med. Imag.*, vol. 1(3),pp. 187-192, 1982.

[4] S. Surti, A. Kuhn, M. E. Werner, A. E. Perkins, J. Kolthammer, and J. S. Karp, "Performance of Philips Gemini TF PET/CT scanner with special consideration for its time-of-flight imaging capabilities." *J. Nucl. Med.*, vol. 48(3), pp. 471-480, 2007.

[5] M. E. Daube-Witherspoon, S. Surti, S. Matej, M. Werner, S. Jayanthi, and J. S. Karp, "Influence of time-of-flight kernel accuracy in TOF-PET reconstruction." in *IEEE Nucl. Sci. Symp. Med. Imag. Conf. Rec.*, 2006, vol. 3, pp. 1723-1727.

[6] J. A. Fessler and W. L. Rogers, "Spatial resolution properties of penalized likelihood image reconstruction: space-invariant tomographs." *IEEE Trans. Image Proc.*, vol. 5(9), pp. 1346-1358, 1996.

[7] J. Qi and R. M. Leahy, "Resolution and noise properties of MAP reconstruction for fully 3-D PET." *IEEE Trans. Med. Imag.*, vol. 19(5), pp. 493-506, 2000.

[8] K. Vunckx, D. Bequé, M. Defrise, and J. Nuyts, "Single and multipinhole collimator design evaluation method for small animal SPECT." *IEEE Trans. Med. Imag.*, in press.

[9] M. H. Hudson and R. S. Larkin, "Accelerated image reconstruction using ordered subsets of projection data." *IEEE Trans. Med. Imag.*, vol. 13(4), pp. 601-609, 1994.

[10] M. Conti, "Effect of randoms on signal-to-noise ratio in TOF PET." *IEEE Trans. Nucl. Sci.*, vol. 53(3), pp. 1188-1193, 2006.

[11] Y. Zhang-O'Connor and J. A. Fessler, "Fast predictions of variance images for fan-beam transmission tomography with quadratic regularization." *IEEE Trans. Med. Imag.*, vol. 26(3), pp. 335-346, 2007.

[12] S. Vandenberghe, S. Matej, M. E. Witherspoon, J. S. Karp, and I. Lemahieu, "Determining timing resolution from TOF-PET emission data." presented at *IEEE NSS-MIC 2007*, M08-4.